energies

MDPI

Article

Wave Energy Conversion Performance of an OWC System with Coupled Pneumatic Damping

Xiang Rao [1,2], Yin Ye [1,2], Yaqun Zhang [1,2,*], Wenshi Cui [1,2,3] and Songwei Sheng [1,2]

[1] Guangzhou Institute of Energy Conversion, Chinese Academy of Sciences, Guangzhou 510640, China; raoxiang0620@mail.ustc.edu.cn (X.R.)
[2] CAS Key Laboratory of Renewable Energy, Guangzhou 510640, China
[3] College of Energy Science and Technology, University of Science and Technology of China, Hefei 230026, China
* Correspondence: zhangyq@ms.giec.ac.cn

Abstract

Improving the conversion of incident wave energy into useful pneumatic power requires a clear understanding of the coupling among floating body motions, internal water column oscillation, air compression, and pneumatic damping in oscillating water column (OWC) systems. In this study, a coupled multi degree of freedom (MDOF) analytical framework is developed by incorporating the surge, heave, and pitch motions of the floating body together with internal water column oscillation and compressible chamber air dynamics. A distinctive feature of the framework is the direct comparison between a simplified single degree of freedom (SDOF) configuration and the coupled MDOF configuration, which enables the contribution of body motion coupling to pneumatic energy conversion to be explicitly identified. Based on potential flow theory, frequency-domain hydrodynamic characteristics are coupled with the pneumatic response to evaluate added mass, radiation damping, hydrodynamic impedance, chamber pressure, pneumatic power, and capture width ratio (CWR). The MDOF results exhibit two distinct pneumatic power peaks. The dominant peak reaches a non-dimensional pneumatic power coefficient P^* of approximately 0.88 at $\omega \approx 0.4$ ($kh \approx 0.13$), whereas a secondary peak of approximately 0.06 appears in the higher frequency regime ($kh \approx 2.2$), reflecting the primary water column resonance and the contribution of coupled structural responses, respectively. Comparison with wave-basin measurements reproduces the principal CWR trend and resonance peak location, although the peak magnitude is overpredicted near resonance. The results clarify how body motion coupling and pneumatic damping jointly govern the transfer of incident wave energy into pneumatic power and provide a practical framework for resonance tuning and preliminary performance optimization of OWC systems.

Keywords: wave energy conversion; oscillating water column; hydrodynamics; pneumatic power; capture width ratio

Academic Editor: Lars Johanning

Received: 22 July 2026
Revised: 19 August 2026
Accepted: 22 August 2026
Published: 27 August 2026

1. Introduction

The efficient exploitation of ocean energy is a major objective in the development of wave energy conversion technologies [1]. Among the available concepts, the OWC is one of the most widely investigated [2]. Incident waves drive oscillation of the internal water column, causing alternating compression and expansion of the chamber air and thereby converting wave-induced mechanical energy into pneumatic energy [3].

Over the past few decades, OWC technology has been extensively explored as a promising solution for wave energy conversion. Fixed-bottom OWC devices, in particular, have been widely studied because of their structural simplicity and ease of integration with coastal infrastructure. Their hydrodynamic behavior, chamber pressure dynamics, and energy conversion performance have been investigated using analytical, numerical, and experimental approaches [4–6]. In parallel with improvements in hydrodynamic modeling, geometric design has been recognized as another important factor governing OWC performance. A recent systematic review of Constructal Design applications to wave energy converters identified OWC devices as the most frequently studied converter type and showed that geometric degrees of freedom can strongly influence hydropneumatic performance [7]. For example, Constructal Design studies have demonstrated that chamber aspect ratio and submergence can materially alter the hydrodynamic power of an OWC [8]. These studies emphasize the importance of geometry; the present work, however, keeps the device geometry prescribed and focuses on the dynamic coupling among body motion, internal water column oscillation, and pneumatic damping.

Numerous experimental prototypes and full-scale facilities have also demonstrated the feasibility of OWC technology in practical marine environments [9–12]. Various air turbine concepts, including Wells and impulse turbines, have been implemented and optimized to improve pneumatic power extraction. Brito Melo et al. [13], for example, analyzed the sensitivity of OWC performance to Wells turbine design parameters, while Liu et al. [14] investigated the unsteady performance and self-starting behavior of an axial flow impulse turbine under reciprocating airflow. Although these studies have established a strong basis for fixed OWC systems, offshore floating configurations introduce additional hydrodynamic degrees of freedom and therefore more complex energy transfer mechanisms.

Floating OWCs are increasingly considered for offshore wave energy harvesting, particularly in deep-water regions where bottom-fixed installations may be uneconomical. Floating configurations provide deployment flexibility and access to energetic offshore wave climates [15,16], but their rigid-body motions directly affect the relative displacement between the device and the internal water column. Manimaran [17] showed that the hydrodynamic response of floating OWC and BBDB concepts depends strongly on their coupled motion characteristics. Wang et al. [18] further demonstrated that hydrodynamic interaction and relative positioning can enhance the performance of a dual OWC system, while Gadelho et al. [19] experimentally showed that chamber damping can significantly modify the motions and internal free-surface response of a backward bent duct buoy (BBDB). Related confined-fluid resonance studies, although based on different structural configurations, also show that allowing heave or floater motion can shift resonant conditions and modify wave loads, and that nonlinear focused wave groups can trigger pronounced transient resonance [20–22]. These observations reinforce the importance of explicitly accounting for structural motion when interpreting resonance and energy transfer behavior in floating OWC systems. Floating systems are also sensitive to mooring, stability, and coupled hydrodynamic–pneumatic effects [23].

Floating OWCs can exhibit nonlinear behavior because structural dynamics, hydrodynamic forces, internal water column oscillation, and chamber air compressibility interact simultaneously [24]. Under irregular or strongly transient waves, nonlinear free-surface effects, turbulence, and wave–structure interaction can further influence the response. Rezanejad et al. [25] experimentally demonstrated that the configuration of a floating dual-chamber OWC substantially affects its motion and conversion performance. Resonance between platform motions and the internal water column can lead to multimodal excitation and either amplify or suppress energy capture depending on the tuning condition [26]. In addition, compressible airflow introduces pressure drop and transient flow effects that complicate prediction of pneumatic power, particularly near rapid flow reversals [27]. Accordingly, simplified models must be applied with a clear understanding of the physical effects they retain and those they neglect.

Many theoretical and numerical OWC models therefore rely on idealizations such as linearized free-surface conditions, simplified PTO damping, or reduced sets of rigid-body modes [28,29]. Liu et al. [30] developed an integrated chamber–turbine model to reduce errors associated with decoupled air–water dynamics. Abbasnia et al. [31] subsequently developed a fully nonlinear two-dimensional potential flow framework with compressible chamber pressure, with emphasis on resolving nonlinear free-surface evolution and chamber–flow interaction. Chen and Wu [32], by contrast, developed a frequency-domain potential flow solution method capable of evaluating radiation, diffraction, and frequency-dependent hydrodynamic coefficients, while Chen et al. [33] applied related hydrodynamic modeling to a BBDB configuration. Hybrid frequency–time formulations have also been used to connect frequency-domain hydrodynamic data with time-domain dynamic response [34,35]. These approaches provide important high fidelity or specialized capabilities, but their objectives differ from the system-level coupling analysis pursued here.

The present study therefore develops a coupled analytical framework for a floating OWC in which the surge, heave, and pitch motions of the body are combined with internal water column oscillation and compressible chamber air dynamics. The main contributions are threefold. First, the model organizes hydrodynamic, pneumatic, and structural effects within a unified frequency and time-domain formulation. Second, SDOF and MDOF configurations are compared directly to isolate the influence of body motion coupling on chamber pressure, hydrodynamic impedance, pneumatic power, and CWR. Third, the model identifies a dominant and a secondary pneumatic power peak and evaluates the predicted resonance behavior against published wave-basin measurements. The aim is not to replace fully nonlinear or CFD approaches for resolving local viscous flow structures, but to provide a compact system-level framework for interpreting resonance, pneumatic damping, and preliminary OWC performance.

2. Analytical Framework

2.1. Mathematical Model

Establishing an appropriate mathematical model is essential for ensuring the accuracy of subsequent analyses. For example, in the study by Kim et al. [36], a two-dimensional mathematical model was developed to simulate the behavior of a BBDB in a wave flume, providing valuable insights into the hydrodynamic performance of the device.

The present study adopts a reduced-order potential flow formulation rather than a computational fluid dynamics (CFD) model; consequently, the Navier–Stokes equations are not solved directly. The water domain is treated as inviscid, incompressible, and irrotational, so the fluid motion is represented by a velocity potential satisfying the Laplace equation. Frequency-domain potential flow analysis supplies the wave excitation, added mass, and radiation damping terms, which are assembled into the SDOF and MDOF equations of motion. The body and internal water column responses are then coupled with the chamber pressure evolution and nonlinear orifice flow relation. The resulting equations are integrated in the time domain by the Newmark β scheme with an iterative pressure–motion coupling procedure. The formulation was implemented through an in-house numerical routine rather than a CFD solver, and its system-level response is assessed against the physical model data described in Section 3.3.

The mathematical model of the coupled OWC system is schematically represented in Figure 1. The overall fluid domain is decomposed into three subdomains: the exterior wave field (Ω_1), the flume domain beneath the OWC (Ω_2), and the internal air chamber region (Ω_3). These subdomains are bounded by distinct interfaces, including the external free surface (S_{f1}), the internal air–water interface (S_{f2}), and the impermeable boundaries such as the side walls and the seabed (S_{w_out}, S_{b1}, S_{b2}, and S_d). The upper boundary of the air chamber, denoted as S_{out}, corresponds to the outlet through which airflow is exchanged with the atmosphere, typically representing the orifice. Under incident wave excitation from the open sea, the water column inside the chamber oscillates vertically, inducing a reciprocating airflow in the compressible air volume above. This configuration forms the basis for developing the governing equations that describe the coupled hydrodynamic and thermodynamic processes of the system.

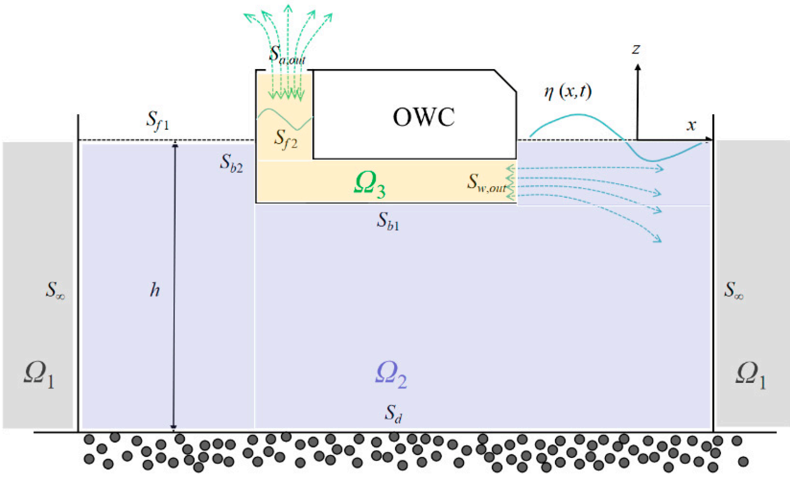

Figure 1. The mathematical model.

2.2. Governing Equations and Boundary Conditions

Flow Field Description

For the wave–structure interaction analysis, the water is assumed to be inviscid, incompressible, and irrotational. Under these assumptions, the fluid motion is represented by a scalar velocity potential $\varphi(x,z,t)$, which is decomposed into incident, diffraction, and radiation components:

$$\begin{aligned}\phi(x,z,t) &= \phi^{inc} + \phi^{diff} + \phi^{rad} \\ &= \phi^{inc} + \phi^{diff} + \sum_{j=1}^{6} \dot{X}_j(t)\phi_j^{rad}\end{aligned} \quad (1)$$

where ϕ^{inc} is the incident wave potential, representing the incoming waves generated far from the structure; ϕ^{diff} is the diffraction potential, induced by the scattering of incident waves due to the presence of the structure; ϕ_j^{rad} are the radiation potentials associated with unit velocity in the j th degree of freedom (j = 1, 2, . . ., 6), corresponding to the surge, sway, heave, roll, pitch, and yaw motions, respectively.

Each component satisfies the Laplace equation within the fluid domain $\Omega_1 \cup \Omega_2$. The respective boundary conditions are defined over multiple surfaces, including the free surface, air–water interface, impermeable walls, and the body's wetted surface. Each component satisfies the Laplace equation:

$$\nabla^2\phi^i = 0 \quad i \in (inc, diff, rad) \qquad \forall(x,z) \in \Omega_1 \cup \Omega_2 \quad (2)$$

On the free-surface S_{f1}, the linearized kinematic and dynamic conditions are imposed and combined into a single boundary condition:

$$\frac{\partial^2\phi^i}{\partial t^2} + g\frac{\partial\phi^i}{\partial z} = 0 \quad z = 0 \quad (3)$$

At the internal water–air surface S_{f2}, the vertical velocity of the free surface equals the velocity of the internal water column, denoted as $\xi(t)$. The dynamic boundary condition accounts for the pressure jump across the air–water interface:

$$\frac{\partial\phi}{\partial t} + g\xi(t) = -\frac{p(t)}{\rho} \tag{4}$$

$$\frac{\partial\phi}{\partial z} = \frac{d\xi(t)}{dt} = \dot{\xi}(t) \tag{5}$$

On the impermeable boundaries, including the tank walls and bottom surfaces S_{b1}, S_{b2}, and S_d, the Neumann type no flow condition is enforced:

$$\frac{\partial\phi^{diff}}{\partial n} = 0 \tag{6}$$

$$\frac{\partial\phi^{rad}}{\partial n} = \mathbf{n}\cdot\mathbf{V}(t) = \sum_{j=1}^{6} n_j\dot{X}_j(t) \tag{7}$$

These boundary conditions ensure that each potential component satisfies its own physical excitation mechanism. The chamber is open to the atmosphere via the outlet surface $S_{a,out}$, which represents the turbine exhaust interface. The boundary condition at $S_{a,out}$ governs the airflow rate through the orifice, modeled non linearly as:

$$Q(t) = C_d A_w \mathrm{sign}(p(t)) \cdot \sqrt{\frac{2|p(t)|}{\rho_a}} \tag{8}$$

where $Q(t)$ is the volumetric airflow rate through the orifice; C_d is the discharge coefficient accounting for non-ideal flow through the orifice, C_d = 0.9; $p(t)$ is the air pressure inside the chamber; A_w is the effective cross sectional area of the exhaust orifice, (=1133.54 mm^2); and ρ_a is the air density (=1.225 $\mathrm{kg/m}^3$).

2.3. Hydrodynamic Forces

The hydrodynamic forces acting on the floating body and the internal water column are obtained, and key coefficients such as added mass and radiation damping are derived. These quantities are essential for establishing the motion equations in the frequency and time domains. From the unsteady Bernoulli equation, the pressure field is

$$p = -\rho\left(\frac{\partial\phi}{\partial t} + gz\right) \tag{9}$$

The hydrodynamic force in the j th direction on the OWC system surface (S_{b1} and S_{b2}) is computed by integrating the pressure over the wetted surface:

$$F_j^{exc}(t) = \int_{S_{b1}\cup S_{b2}} p n_j dS \tag{10}$$

In the frequency domain, the radiation force due to motion is given by:

$$F_j^{exc}(\omega) = \int_{S_{b1}\cup S_{b2}} p^{inc}(x,y,z,\omega) n_j dS \tag{11}$$

The formulation of force due to body motion introduces the added mass $m_j(\omega)$ and damping $c_j(\omega)$:

$$F_j^{rad}(\omega) = -\omega^2 m_j(\omega) X_j(\omega) - i\omega^2 c_j(\omega) X_j(\omega) \tag{12}$$

2.4. Coupled System Dynamics

The coupled OWC system is analyzed using two configurations with different levels of physical complexity. In the SDOF configuration, all external rigid-body motions are constrained and only the vertical oscillation of the internal water column is retained; this displacement is denoted by x_w. In the MDOF configuration, the floating body is allowed to move in surge (x_1), heave (x_3), and pitch (x_5), while the internal water column simultaneously oscillates in the vertical direction (x_w). Thus, the MDOF generalized coordinate vector is $x = [x_1, x_3, x_5, x_w]^T$. This definition clearly separates the rigid-body heave x_3 from the internal water column coordinate x_w and enables the effect of body motion coupling on pneumatic energy conversion to be assessed systematically.

For the SDOF configuration, only the internal water column coordinate x_w is retained. The governing equation of motion is

$$-\omega^2\left(\mathbf{m}_j+\mathbf{m}_a\right)x_w''(t)+i\omega\left(\mathbf{b}_j+\mathbf{b}_p\right)x_w'(t)+\mathbf{c}_j x_w(t)=\mathbf{F}_j^{exc} \tag{13}$$

where m_a, b_p, and c_j denote the added mass, pneumatic damping, and hydrostatic restoring terms, respectively, and characterize the dynamic response of the retained internal water column degree of freedom.

Using x_w as the SDOF displacement, the impedance $\mathbf{Z}(\omega)$ is defined as:

$$\mathbf{Z}(\omega)=-\omega^2\left(\mathbf{m}_j+\mathbf{m}_a\right)+i\omega\left(\mathbf{b}_j+\mathbf{b}_p\right)+\mathbf{c}_j \tag{14}$$

The internal water column displacement can therefore be expressed as a function of wave excitation force and impedance at wave frequency ω:

$$x_w=\mathbf{Z}^{-1}(\omega)\mathbf{F}_j^{exc} \tag{15}$$

Then, the instantaneous pneumatic power can be derived as:

$$P=p(t)Q(t) \tag{16}$$

Thus, considering the Formulas (8), (9), and (16), the average pneumatic power over one wave period is

$$\overline{P}=\frac{C_d A_w}{T}\sqrt{\frac{2}{\rho_a}}\int_{p(t)>0}p^{\frac{3}{2}}(t)dt \tag{17}$$

Assuming that the sinusoidal pressure $p(t) = p_a\sin(\omega t)$, the time averaged power becomes

$$\overline{P}=\frac{2C_d A_t p_a^{\frac{3}{2}}}{3\pi\omega}\sqrt{\frac{2}{\rho_a}} \tag{18}$$

The pressure amplitude p_a is linked to the internal water column displacement x_w through the pressure evolution equation:

$$\frac{dp_a}{dt}=\frac{p_0 A_w}{V_0}x_w'-\frac{p_a}{V_0}Q(t) \tag{19}$$

In the MDOF configuration, the floating body undergoes surge (x_1), heave (x_3), and pitch (x_5), while the internal water column is represented independently by x_w. The generalized coordinate vector is

$$\mathbf{x}=[x_1,x_3,x_5,x_w]^T \tag{20}$$

The coupled frequency-domain equations of motion are:

$$\mathbf{Z}(\omega) \cdot \mathbf{x} = \mathbf{F}^{exc}(\omega) \tag{21}$$

The internal water column displacement is taken as the fourth component of x:

$$x_w(\omega) = \left[\mathbf{Z}^{-1}(\omega)\right]_4 \cdot \mathbf{F}^{exc}(\omega) \tag{22}$$

Then, the pressure response is given by:

$$p_a(\omega) = i\omega \frac{p_0 A_w}{V_0} x_w(\omega) \tag{23}$$

By combining Equations (20)–(24), the expression for the pneumatic power of the OWC system under MDOF motion can be finally derived as:

$$\overline{P} = \frac{2C_d A_w}{3\pi\omega} \sqrt{\frac{2}{\rho_a}} \left| \sum_{j=1,3,5} \frac{F_j^{exc}}{Z_j(\omega)} \right|^{\frac{3}{2}} \tag{24}$$

The SDOF and MDOF formulations serve complementary purposes. The SDOF model retains only x_w and therefore isolates the water column–air interaction without rigid-body motion. The MDOF model additionally includes body surge x_1, heave x_3, and pitch x_5, allowing direct assessment of how floating body motion changes chamber pressure and pneumatic power. Comparing the two configurations therefore provides a consistent measure of the influence of fluid–structure–air coupling on wave energy conversion.

2.5. Hydrodynamic Analysis and Solution

To generalize the analysis and enable comparative evaluation across different configurations and sea states, several non-dimensional coefficients are defined based on the governing parameters introduced above. These non-dimensional quantities provide insights into the relative significance of hydrodynamic and pneumatic contributions to the energy conversion process and facilitate performance comparison under various design and wave conditions:

$$m^* = \frac{m_j}{\rho l^3} \tag{25}$$

$$c^* = \frac{c_j}{\rho l^3 \omega} \tag{26}$$

$$Z^* = m^* + ic^* \tag{27}$$

$$P^* = \frac{\overline{P}}{\rho g l^3 \omega^3} \tag{28}$$

where l is the chamber water depth; m^* is the non-dimensional added mass coefficient; c^* is the non-dimensional radiation damping coefficient; Z^* is the non-dimensional hydrodynamic impedance coefficient; and P^* is the non-dimensional pneumatic power coefficient.

To incorporate the effect of air pressure coupling with its motion, the air-induced feedback force vector is defined as:

$$\mathbf{F}_{air}(p_a) = [p_a(t), p_a(t), p_a(t), -A_w p_a(t),]^T \tag{29}$$

Then the MDOF dynamic system is written as:

$$-\omega^2(\mathbf{m}_j + \mathbf{m}_a)\mathbf{x}'' + i\omega(\mathbf{b}_j + \mathbf{b}_p)\mathbf{x}' + \mathbf{c}_j\mathbf{x} = \mathbf{F}_j^{exc} + \mathbf{F}_{air}(p_a) \tag{30}$$

The added mass, radiation damping, and hydrostatic restoring terms used in the coupled equations are obtained from the frequency-domain potential flow formulation. Because these hydrodynamic coefficients are frequency dependent, the coefficients corresponding to each prescribed regular wave frequency are used for that wave condition and are kept constant during the associated time-domain integration. This frequency by frequency transfer of hydrodynamic data avoids treating a single coefficient set as representative of the entire frequency range and provides a consistent link between the frequency-domain hydrodynamic solution and the time-domain pneumatic coupling [37,38].

The time-domain equations for the body motions and internal water column are coupled with the compressible air model and discretized using the second order implicit Newmark β scheme. At each time step, the displacement and chamber pressure variables are updated iteratively through the residual and Jacobian relations given below. This procedure resolves the nonlinear pressure–orifice flow feedback while retaining the hydrodynamic coefficients associated with the prescribed wave frequency.

$$\mathbf{x}_{n+1} = \mathbf{x}_n + \Delta t \mathbf{x}_n' + \Delta t^2 \left[\left(\frac{1}{2} - \beta \right) \mathbf{x}_n'' + \beta \mathbf{x}_{n+1}'' \right] \tag{31}$$

This method leads to nonlinear residuals:

$$\text{Res}^{(k)} = -\omega^2 (\mathbf{m}_j + \mathbf{m}_a) \mathbf{x}''^{(k)} + i\omega (\mathbf{b}_j + \mathbf{b}_a) \mathbf{x}'^{(k)} + \mathbf{c}\mathbf{x}^{(k)} - \mathbf{F}^{exc} - \mathbf{F}_{air}^{(k)} \tag{32}$$

At each time step, iteration is employed. The Jacobian matrix:

$$\mathbf{J}^{(k)} = \begin{bmatrix} \frac{\partial \text{Res}}{\partial \mathbf{x}} & \frac{\partial \text{Res}}{\partial (p_a)} \\ \frac{\partial (p_a')}{\partial \mathbf{x}} & \frac{\partial (p_a')}{\partial (p_a)} \end{bmatrix} \tag{33}$$

Update values computed as:

$$\begin{bmatrix} \delta \mathbf{x} \\ \delta p_a \end{bmatrix} = -\left(\mathbf{J}^{(k)} \right)^{-1} \begin{bmatrix} \text{Res}^{(k)} \\ p_a'^{(k)} - p_t \end{bmatrix} \tag{34}$$

At each iteration, the air pressure rate mismatch is evaluated together with the displacement correction. Convergence is accepted when both $||\delta x|| < 10^{-6}$ and $||\delta p_a|| < 10^{-6}$. These tolerances are applied consistently to all cases. Because the present framework is an analytical/potential flow model rather than a CFD simulation, no spatial CFD mesh is involved in this solution procedure.

3. Results and Discussion

The theoretical results are compared with the published physical model measurements of the pentagonal BBDB reported by Wu et al. [39], the concrete model was showed in Figure 2. The validation data were obtained from three-dimensional regular wave-basin tests in which incident wave height and period, internal water surface elevation, and the pressure difference between the inside and outside of the air chamber were measured. The principal parameters of the physical model are summarized in Table 1.

Considering the dispersion relation:

$$\omega^2 = gk\tanh(kh) \tag{35}$$

The calculated results originally presented as functions of wave frequency ω can also be transformed into functions of the relative water depth kh for further analysis.

Figure 2. The concrete OWC model.

Table 1. Principal parameters of the physical model from literature [39].

Parameter	Symbol	Value
Water depth	h	0.75 m
Model mass	M	30 kg
Nozzle diameter	D_n	45 mm
Nozzle area	A_n	1.59×10^{-3} m^2
Mooring chain length	L_m	1.23 m
Incident wave height	H	0.10 m

In order to measure the ability of OWC to convert wave power into pneumatic power, the expression for CWR is defined as:

$$CWR = \frac{P_{air}}{P_{reg}} \times 100\% \quad (36)$$

where P_{air} is the pneumatic power, and P_{reg} is the regular incident wave power, derived as:

$$P_{reg} = \frac{1}{16}\rho g H^2 B \frac{\omega}{k}\left(1 + \frac{2kh}{\sinh(2kh)}\right) \quad (37)$$

where B is the reference width of the OWC normal to the direction of wave propagation. Accordingly, P_{reg} represents the total incident wave power available over the reference width B, rather than the wave power per unit crest width. With this definition, a CWR above 100% does not imply that the device extracts more energy than is available in the surrounding wave field. Rather, it indicates that, near resonance, the effective hydrodynamic capture width is greater than the selected geometrical reference width B because of diffraction, radiation, and resonant wave–body interaction.

3.1. SDOF Mode

Figure 3 shows the four non-dimensional SDOF coefficients as functions of wave frequency over $0 < \omega \leq 6$. The added mass coefficient m^* initially increases and reaches a local maximum near $\omega \approx 1.8$, then decreases over the intermediate frequency range before rising slightly again for $\omega > 4$. The radiation damping coefficient c^* decreases to a minimum in the mid-frequency range, indicating reduced radiative resistance there. The magnitude of the hydrodynamic impedance Z^* varies smoothly as the combined influence of inertia and damping changes with frequency. Most notably, the pneumatic power coefficient P^* exhibits a pronounced maximum near $\omega \approx 2.5$. Away from this resonance band, P^* decreases rapidly, indicating a substantially weaker pneumatic response at both sub-resonant and super-resonant frequencies.

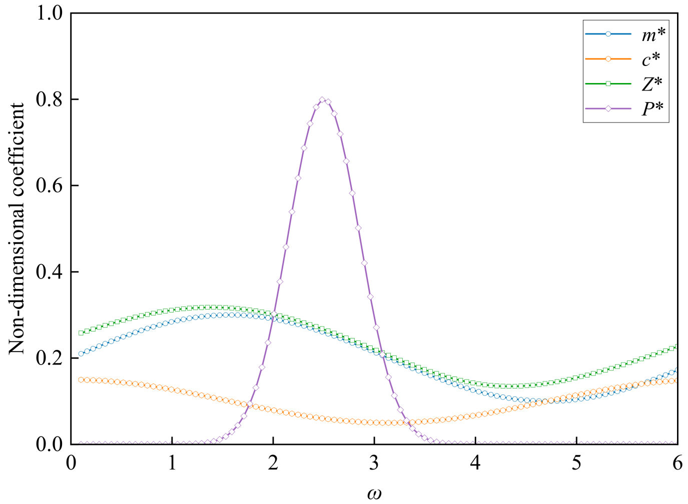

Figure 3. Variations in the dimensionless SDOF with ω.

As shown in Figure 4, the behavior of the added mass coefficient m^* demonstrates a classical decay with increasing kh, dropping from a value of approximately 0.55 at low wavenumbers to around 0.11 when $kh = 6$. This decline highlights the reduced influence of surrounding fluid inertia at higher frequencies, where the wavelength becomes much shorter relative to the model scale. In contrast, the damping coefficient c^* rises monotonically over the entire range of kh, indicating a progressively stronger wave radiation effect. Such growth is consistent with the increasing energy dissipation associated with shorter wavelength interactions. Z^* displays a smooth transition: it remains elevated in the intermediate range of $kh \in [2,4]$, suggesting enhanced hydrodynamic responsiveness.

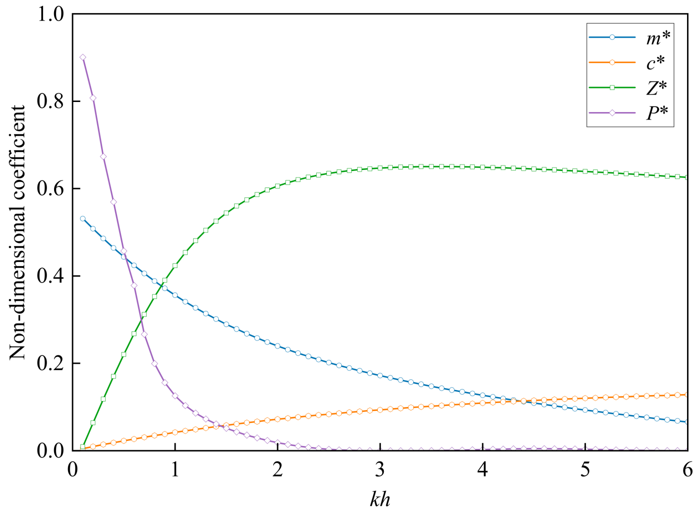

Figure 4. Variations in the dimensionless SDOF with kh.

Of particular interest is the trend of the dimensionless pneumatic power coefficient P^*, which declines consistently over the entire range of kh, with its maximum occurring at the minimum kh value. This downward trend in P^* highlights a critical physical insight: as wavenumbers increase (i.e., wavelengths shorten), the interaction between wave-induced motion and the internal air compression becomes weaker, leading to diminished airflow and reduced energy conversion. The result implies that, for the given chamber geometry and turbine characteristics, the floating OWC is best tuned for longer waves, and efficiency drops significantly as wave periods decrease.

3.2. MDOF Mode

As the frequency increases, the non-dimensional added mass coefficients m^* associated with the four motion modes exhibit distinct dynamic characteristics, shown in Figure 5. In the surge direction (x_1), the coefficient rises progressively, reflecting the intensifying inertia-induced by accelerating horizontal wave motion. The heave component (x_3) decreases from 0.45 to 0.33 as ω rises from 0.1 to 3.2, then climbs as ω increases. The pitch mode (x_5) displays an oscillatory behavior rather than a monotonic trend, fluctuating between 0.37 and 0.52. This pattern suggests that the rotational added mass is sensitive to frequency-dependent wave excitation, possibly due to the interaction between wave moments and geometry. Meanwhile, the water column mode (x_w) maintains near constancy across the frequency spectrum, implying its behavior is dominated by internal air compressibility rather than hydrodynamic radiation.

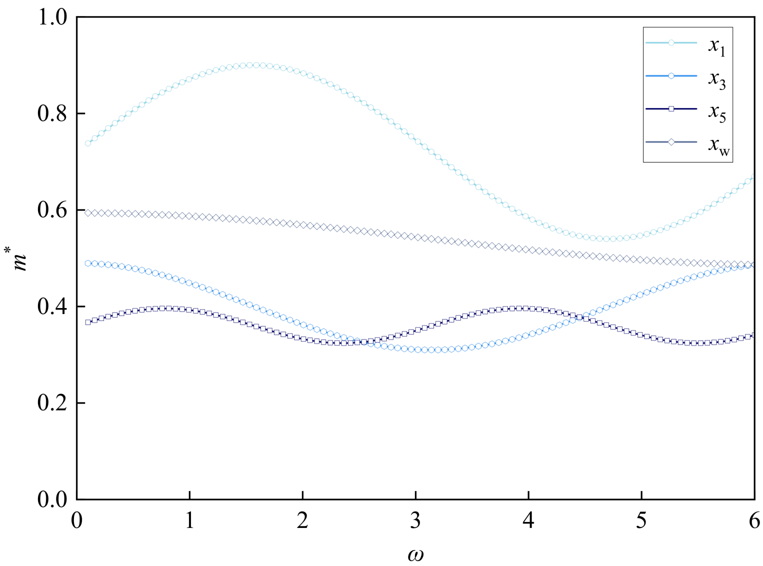

Figure 5. Variation m^* of MDOF with ω.

Figure 6 compares m^* for four degrees of freedom as a function of kh. For the surge mode (x_1), m^* exhibits a distinct peak near kh = 0.8, followed by a gradual decline to a minimum at kh = 2.0, and then increases again. In the heave direction (x_3), m^* reaches its lowest value at 1.0 and increases steadily thereafter, indicating enhanced vertical inertia due to stronger wave–body interaction at higher wavenumbers. For the pitch mode (x_5), the coefficient decreases continuously from 0.2 to 0.1 with increasing kh. This trend confirms that shorter waves produce smaller hydrodynamic moment arms, thereby reducing the rotational added mass. The change of x_5 shows a monotonic increase, highlighting that wave confinement becomes stronger at higher kh, intensifying the effective inertia of the oscillating water column within the chamber.

At low frequencies (ω < 1.0), all four modes exhibit relatively high values of c^*, particularly in the surge and pitch directions, as shown in Figure 7. This is attributed to the fact that, at low wave frequencies, the wavelength becomes much larger than the OWC dimensions, resulting in slow but large-amplitude fluid motion. The body's motion generates significant wave radiation resistance to maintain continuity, especially in surge and pitch, where horizontal and rotational water movements dominate. Such behavior enhances energy dissipation, leading to high damping coefficients.

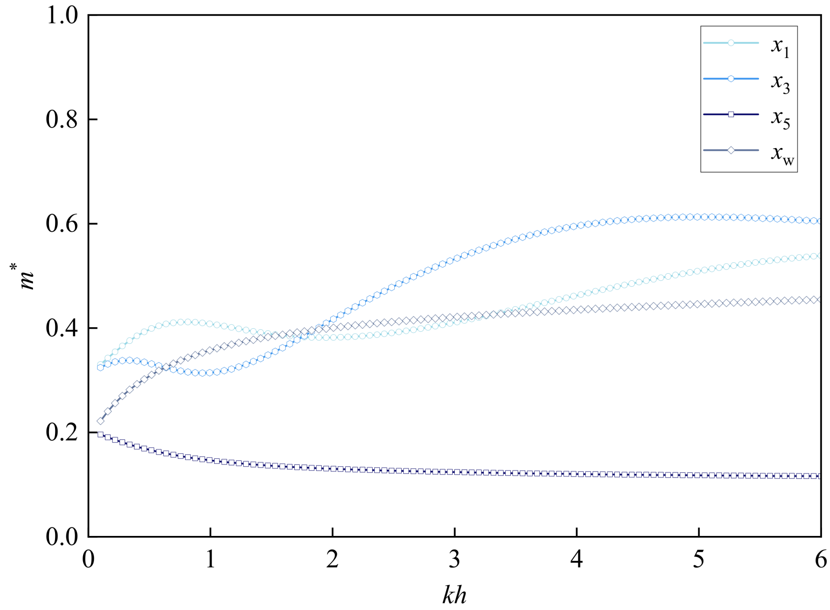

Figure 6. Variation m^* of MDOF with kh.

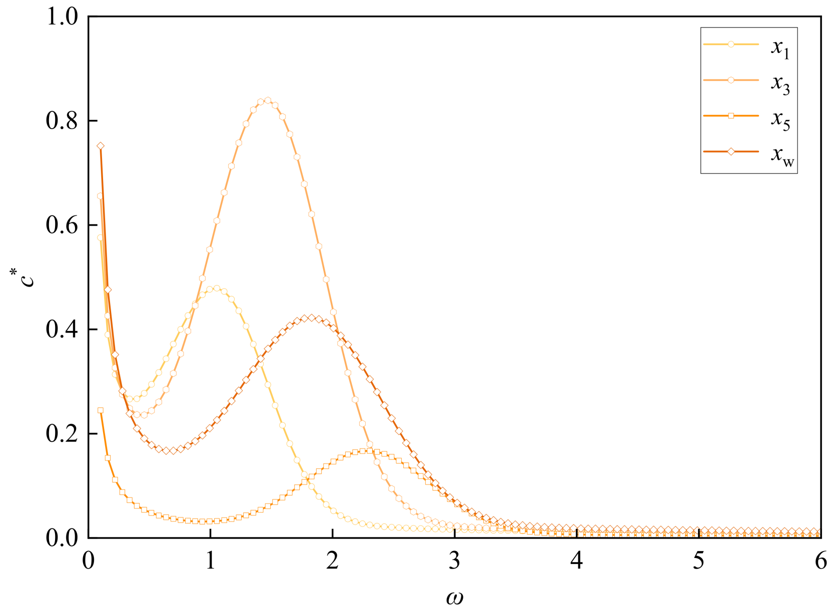

Figure 7. Variation c^* of MDOF with ω.

As ω increases, the damping coefficients for x_1, x_3, and x_5 decrease initially due to the diminishing effectiveness of long-wave radiation. Subsequently, each mode displays a localized minimum or inflection point, followed by a moderate increase or plateau. The damping of x_w shows a more monotonic decreasing pattern, reflecting the reduced interaction time between the oscillating interface and the compressible air chamber at higher frequencies.

The variation of dimensionless damping coefficients c^* with kh reveals insightful frequency–depth coupling effects across the four degrees of freedom, as shown in Figure 8. All four curves initially increase and then decline with rising kh, reflecting frequency-selective radiation characteristics of the OWC. For surge (x_1), the curve peaks at $kh \approx 3.7$ and then declines. Heave (x_3) increases and reaches a local maximum at $kh \approx 4.2$. Pitch (x_5) shows a sharp peak at $kh \approx 2.8$. Water column motion (x_w) grows monotonically and peaks near $kh \approx 5.0$, indicating intensified air–water exchange.

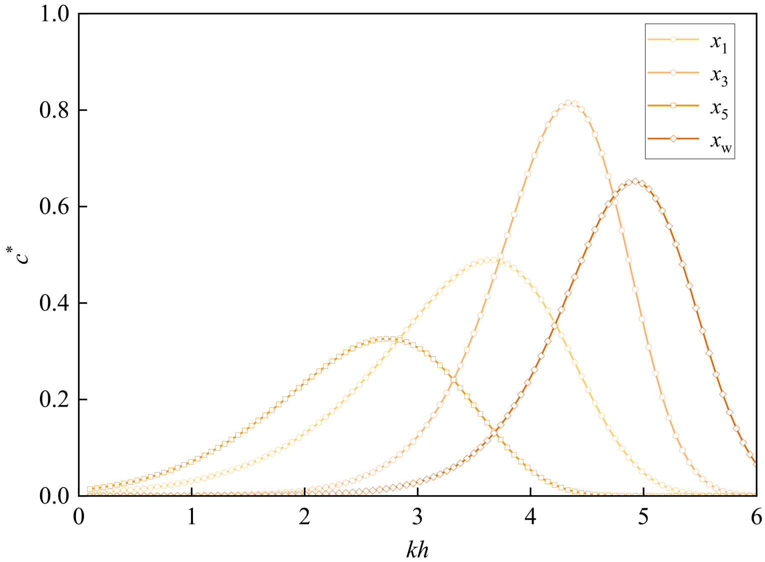

Figure 8. Variation c^* of MDOF with kh.

At low frequencies ($\omega < 0.5$), all four curves exhibit the high initial values shown in Figure 9, primarily driven by the dominant contribution of radiation damping over added mass in this regime. This behavior is physically consistent with the fact that at low frequencies, the system responds more sluggishly, and energy dissipation through wave radiation becomes relatively more significant than inertial effects. For surge (x_1), heave (x_3), and water column motion (x_w), Z^* increases rapidly beyond $\omega = 0.5$, reaching peak values between $\omega = 1.5$ and $\omega = 2.0$, followed by a gradual decrease. This behavior reflects resonance characteristics in these modes, where both radiation damping and added mass synergistically enhance the system's dynamic resistance at specific frequency bands. In contrast, the pitch mode (x_5) shows a relatively flat Z^* profile, fluctuating mildly around 0.4 across the entire frequency range. This indicates that pitch motion is less sensitive to frequency-dependent hydrodynamic effects, likely due to the geometric symmetry and shorter moment arm involved in rotational excitation.

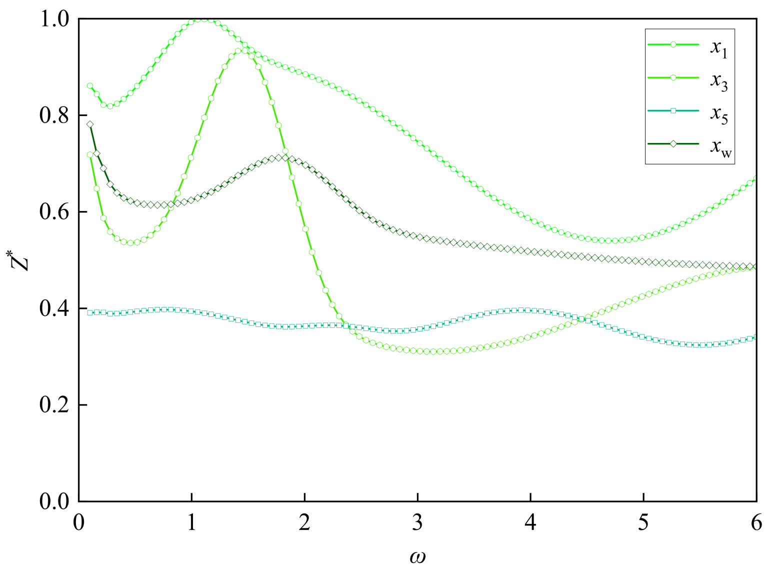

Figure 9. Variation Z^* of MDOF with ω.

Figure 10 illustrates that all four curves exhibit a clear non-monotonic behavior: as kh increases, Z^* first rises, reaches a peak, and then gradually decreases. In the surge direction (x_1), Z^* reaches its maximum near $kh = 3.4$, indicating a strong hydrodynamic resonance influenced by long-wavelength OWC interactions. For the heave mode (x_3), Z^* peaks at kh = 2.5, where the highest overall Z^* is observed, signifying dominant added mass and radiation effects typical of vertical motion in semi-submerged structures. The pitch mode (x_5) peaks earlier at kh = 1.8, yet exhibits the smallest peak magnitude, highlighting weak rotational coupling. In contrast, the internal water column motion (x_w) exhibits a broad and pronounced maximum at kh = 4.2, reflecting intensified coupling with the compressible chamber at high wavenumbers.

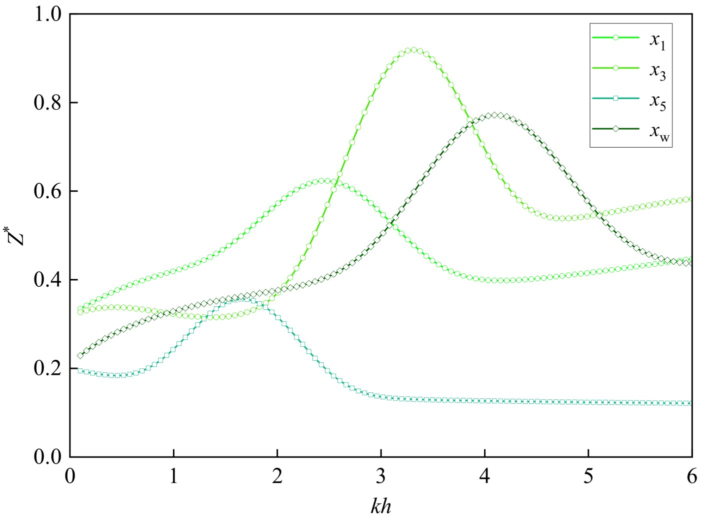

Figure 10. Variation Z^* of MDOF with kh.

Despite the OWC system having only a single chamber, the computed dimensionless pneumatic power coefficient P^* demonstrates a distinct double-peak pattern across the frequency range, as shown in Figure 11. The first and dominant peak, occurring at $\omega \approx 0.4$, corresponds to the natural resonance of the internal water column. The second peak, located at $\omega \approx 4.4$, though significantly smaller in magnitude (about 0.06), reveals an important dynamic phenomenon: at higher frequencies, other structural modes become more active, generating differential pressure that contributes to intermittent airflow and secondary energy transfer. This suggests that even in a single-chamber design, multiple hydrodynamic modes can indirectly modulate the airflow rate, especially under nonlinear response conditions.

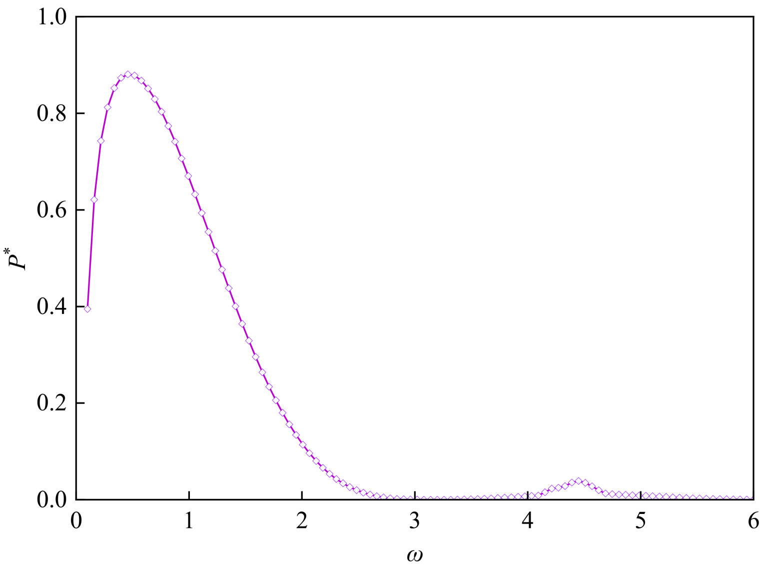

Figure 11. Variation P^* of MDOF with ω.

A detailed inspection of P^* as a function of kh reveals two energetically significant regimes, as shown in Figure 12. The dominant peak at $kh = 0.13$, where $P^* = 0.88$, occurs under long-wave conditions. This suggests a resonance-like phenomenon between the heaving water column and the compressible air chamber, where the large stroke of water motion efficiently pumps air through the orifice. As kh increases, P^* rapidly declines due to reduced wave-induced fluid penetration and diminishing oscillation amplitude. A secondary peak in P^* emerges near $kh = 2.2$, where the coefficient reaches approximately 0.06. This localized peak is attributed to a higher-order resonance condition in which the internal water column oscillation is synchronously amplified by the wave-induced forcing. At this kh, the phase relationship between the water column motion and the air compression reaches a near-optimal condition, resulting in pneumatic output despite the system operating away from the primary resonance.

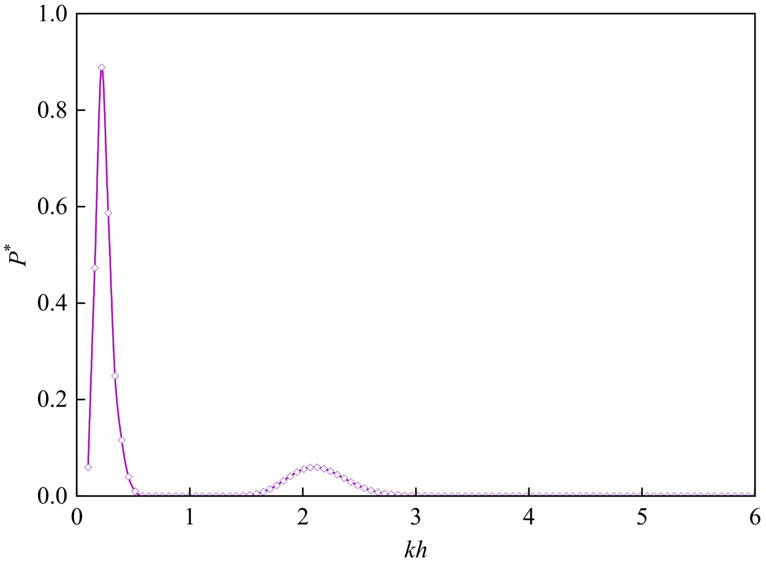

Figure 12. Variation P^* of MDOF with kh.

3.3. Validation Against Physical Model Tests

As shown in Figure 13, the theoretical and experimental CWR curves exhibit the same principal resonance trend: the response rises to a pronounced maximum near the natural period and then decreases on either side of the peak. Quantitatively, the published wave-basin experiment reaches a maximum CWR of approximately 146.8%, whereas the theoretical curve reaches approximately 180% in the present calculation, corresponding to an overprediction of about 23% at the peak. From the discrete points shown in Figure 13, the theoretical maximum occurs at approximately T = 1.30 s and the experimental maximum at approximately T = 1.25 s, giving a peak period shift of about 0.05 s (approximately 4%). At shorter periods (T < 1.1 s), the theoretical CWR approaches zero more rapidly than the measured response.

These discrepancies are primarily associated with the simplifications adopted in the theoretical formulation. The MDOF model retains four coupled generalized coordinates. Chamber air compressibility is represented through the pressure evolution relation and acts as a coupled pneumatic response rather than as an independent mechanical degree of freedom. The hydrodynamic formulation is based on linear potential flow assumptions and therefore does not explicitly resolve viscous damping, vortex shedding, turbulent and local orifice losses, valve hysteresis, or internal sloshing. In addition, the theoretical outlet area used in the present model is not identical to the 45 mm nozzle used in the validation experiment, which is another plausible contributor to the difference in peak magnitude.

https://doi.org/10.3390/en19174021

No damping coefficient or other free parameter was tuned to force agreement with the experimental CWR curve.

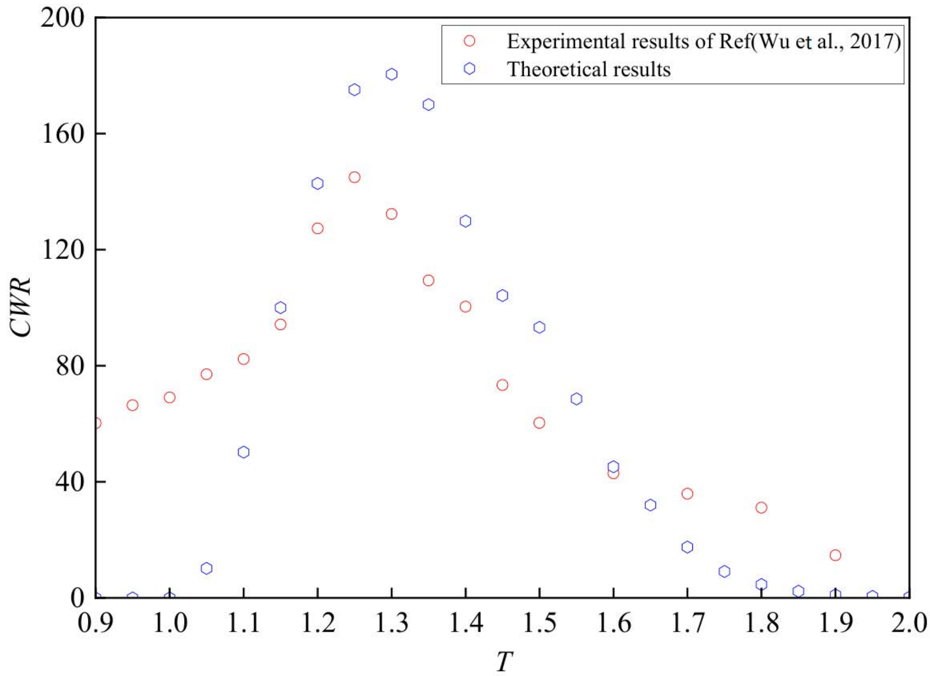

Figure 13. Comparison between the experimental results reported by Wu et al. [39] and the present theoretical results.

Experimental effects can also broaden or suppress the measured resonance peak. The validation study measured incident wave properties, internal water elevation, and chamber pressure difference [39], and unavoidable effects such as wave reflection, sensor calibration, and small geometric or mooring asymmetries may contribute to the observed spread.

Taken together, the agreement in the overall CWR trend and peak period location indicates that the analytical framework captures the dominant resonance mechanism, while the peak magnitude difference defines the present limit of its quantitative accuracy. The model is therefore most appropriate as a design-oriented tool for examining parameter sensitivity, motion coupling, resonance tuning, and preliminary performance trends rather than as a replacement for high-fidelity viscous flow simulations when detailed local losses are required.

3.4. Comparison with Previous Studies

The present results can be placed in context by comparing the objectives of representative OWC modeling approaches. Abbasnia et al. [31] resolved nonlinear free-surface evolution under compressible chamber pressure using a fully nonlinear two-dimensional potential flow model, whereas Chen and Wu [32] focused on a frequency-domain potential flow solution for radiation, diffraction, and hydrodynamic coefficients. The present framework uses a more compact system-level formulation: frequency-dependent hydrodynamic terms are coupled with internal water column motion and chamber pressure dynamics, and SDOF and MDOF configurations are compared directly. Its main benefit is therefore the transparent attribution of changes in pneumatic power and CWR to body motion coupling rather than higher-fidelity resolution of local viscous flow.

The validation against Wu et al. [39] provides an additional experimental benchmark. The analytical model reproduces the principal CWR resonance band and peak period location without parameter fitting, although it overpredicts the peak magnitude. This behavior is consistent with the intended role of the model as a mechanism and design-oriented framework. Moreover, the motion-induced shifts in resonance observed in related heaving and floating body gap resonance studies [20–22] support the broader conclusion that structural motion can alter resonant fluid response; the present OWC results extend this concept to the coupled conversion of wave energy into pneumatic power.

4. Conclusions

This work has established a comprehensive analytical framework for evaluating the hydrodynamic and pneumatic behavior of a floating OWC system equipped with a PTO mechanism. The modeling approach integrates key dynamic components, including the platform's rigid-body motions, the vertical oscillation of the internal water column, and the compressible air dynamics within the chamber. Based on potential flow theory, governing equations are derived and implemented in both frequency and time domains. To facilitate comparative analysis, two configurations are considered: a simplified SDOF model focusing on internal oscillation, and a fully coupled MDOF system capturing body–fluid interactions.

The theoretical results reveal that the non-dimensional pneumatic power coefficient P^* reaches a dominant peak of 0.88 at $\omega = 0.4$ (or $kh = 0.13$) and a secondary peak of 0.06 near $kh = 2.2$, attributed to a higher-order resonance where the internal water column is synchronously amplified by wave-induced forcing, resulting in non-negligible pneumatic output even beyond the primary resonance band. The heave-mode added mass m^* decreases from 0.45 to 0.33 as ω increases, while pitch-mode damping c^* peaks around $kh = 4.2$. Impedance Z^* in surge direction shows maximum resonance at $kh = 3.4$. Comparisons with wave tank experiments demonstrate good agreement in the trend and peak location of the CWR, affirming the model's ability to reproduce dominant resonance behavior.

Despite the use of linear theory, the model omits viscous effects, turbulence, et al., which may cause local deviations from experimental results. Nevertheless, the present framework effectively captures the coupled hydrodynamic–pneumatic mechanisms and provides a useful tool for performance prediction and preliminary design of OWC systems. Future work may extend the model to include nonlinear pneumatic damping behavior, mooring dynamics, and irregular wave input for enhanced accuracy under real-sea conditions.

Author Contributions: X.R.: writing—original draft, experimental arrangement, data processing, and numerical calculation. Y.Y.: funding acquisition and manuscript review. Y.Z.: data verification and manuscript review. W.C.: numerical calculation and data processing. S.S.: manuscript review. All authors have read and agreed to the published version of the manuscript.

Funding: Guangdong Basic and Applied Basic Research Foundation, grant number 2024A1515011282.

Data Availability Statement: The data presented in this study are available from the corresponding author upon reasonable request.

Conflicts of Interest: The authors declare no conflicts of interest.

References

1. Sheng, W. Wave energy conversion and hydrodynamics modelling technologies: A review. *Renew. Sustain. Energy Rev.* **2019**, *109*, 482–498. [CrossRef]
2. Khaleghi, S.; Lie, T.T.; Baguley, C. An overview of the oscillating water column technologies: Issues and challenges. *J. Basic Appl. Sci.* **2022**, *18*, 98–118. [CrossRef]
3. Falcão, A.F.O. Wave energy utilization: A review of the technologies. *Renew. Sustain. Energy Rev.* **2010**, *14*, 899–918. [CrossRef]
4. Sarmento, A.J.; Falcão, A.F.O. Wave generation by an oscillating surface pressure and its application in wave energy extraction. *J. Fluid Mech.* **1985**, *150*, 467–485. [CrossRef]
5. Şentürk, U.; Özdamar, A. Wave energy extraction by an oscillating water column with a gap on the fully submerged front wall. *Appl. Ocean Res.* **2012**, *37*, 174–182. [CrossRef]

6. Zhao, M.; Ning, D. A review of numerical methods for studying hydrodynamic performance of oscillating water column devices. *Renew. Energy* **2024**, 121177. [CrossRef]
7. Capponero, M.E.F.; Telli, G.D.; dos Santos, E.D.; Isoldi, L.A.; Das Neves Gomes, M.; Biserni, C.; Rocha, L.A.O. Constructal Design Method Applied to Wave Energy Converters: A Systematic Literature Review. *Dynamics* **2025**, *5*, 36. [CrossRef]
8. Das N. Gomes, M.; Isoldi, L.A.; Lorenzini, G.; dos Santos, E.D.; Rocha, L.A.O. Constructal Design Applied to the Geometric Evaluation of an Oscillating Water Column Wave Energy Converter Considering Different Real Scale Wave Periods. *J. Eng. Thermophys.* **2018**, *27*, 173–190. [CrossRef]
9. Falcão, A.F.O.; Cândido, J.J.; Justino, P.A.P.; Henriques, J.C.C. Hydrodynamics of the IPS buoy wave energy converter including the effect of non uniform acceleration tube cross section. *Renew. Energy* **2012**, *41*, 105–114. [CrossRef]
10. Fenu, B.; Bonfanti, M.; Glorioso, M.; Pilloton, C.; Bardazzi, A.; Lucarelli, A.; Bracco, G. Experimental investigation of a new hybrid spar buoy wind turbine with oscillating water column. In *OCEANS 2023—Limerick*; IEEE: New York, NY, USA, 2023.
11. Folley, M.; Curran, R.; Whittaker, T. Comparison of LIMPET contra rotating Wells turbine with theoretical and model test predictions. *Ocean Eng.* **2006**, *33*, 1056–1069. [CrossRef]
12. Gato, L.M.C.; Henriques, J.C.C.; Carrelhas, A.A.D. Sea trial results of the biradial and Wells turbines at Mutriku wave power plant. *Energy Convers. Manag.* **2022**, *268*, 115936. [CrossRef]
13. Brito Melo, A.; Gato, L.; Sarmento, A. Analysis of Wells turbine design parameters by numerical simulation of the OWC performance. *Ocean Eng.* **2002**, *29*, 1463–1477. [CrossRef]
14. Liu, Z.; Cui, Y.; Xu, C.; Sun, L.; Li, M.; Jin, J. Experimental and numerical studies on an OWC axial flow impulse turbine in reciprocating air flows. *Renew. Sustain. Energy Rev.* **2019**, *113*, 109272. [CrossRef]
15. Gayathri, R.; Chang, J.Y.; Tsai, C.C.; Hsu, T.W. Wave energy conversion through oscillating water columns: A review. *J. Mar. Sci. Eng.* **2024**, *12*, 342. [CrossRef]
16. Heath, T.V. A review of oscillating water columns. *Philos. Trans. R. Soc. A Math. Phys. Eng. Sci.* **2012**, *370*, 235–245. [CrossRef] [PubMed]
17. Manimaran, R. Comparative evaluation of floating OWC and BBDB wave energy converters by regular and irregular waves using numerical approach. *Ships Offshore Struct.* **2025**, *20*, 1065–1079. [CrossRef]
18. Wang, C.; Deng, Z.; Wang, P.; Yao, Y. Wave power extraction from a dual oscillating water column system composed of heave only and onshore units. *Energies* **2019**, *12*, 1742. [CrossRef]
19. Gadelho, J.; Rezanejad, K.; Xu, S.; Hinostroza, M.; Soares, C.G. Experimental study on the motions of a dual chamber floating oscillating water column device. *Renew. Energy* **2021**, *170*, 1257–1274. [CrossRef]
20. Gao, J.; Mi, C.; Song, Z.; Ma, X. Hydrodynamics of transient gap resonance between a heaving box and a vertical wall excited by focused wave groups. *Ocean Eng.* **2026**, *357*, 125617. [CrossRef]
21. Gong, S.; Gao, J.; Yan, M.; Song, Z.; Shi, H. Effects of floater motion on wave loads during steady state gap resonance occurring between two non identical boxes. *Ocean Eng.* **2025**, *323*, 120649. [CrossRef]
22. Gao, J.; Mi, C.; Song, Z.; Liu, Y. Transient gap resonance between two closely spaced boxes triggered by nonlinear focused wave groups. *Ocean Eng.* **2024**, *305*, 117938. [CrossRef]
23. Rosati, M.; Henriques, J.; Ringwood, J. Oscillating water column wave energy converters: A critical review of numerical modelling and control. *Energy Convers. Manag. X* **2022**, *16*, 100322. [CrossRef]
24. Kelly, T. Experimental and Numerical Modelling of a Multiple Oscillating Water Column Structure. Ph.D. Thesis, National University of Ireland, Maynooth, Ireland, 2018.
25. Rezanejad, K.; Anastas, G.; Hashemzadeh, M.; Gadelho, J.; López, I.; Carballo, R.; Soares, C.G. Experimental study on the hydrodynamic performance of an innovative floating dual chamber oscillating water column. *Ocean Eng.* **2025**, *323*, 120549. [CrossRef]
26. Farshforoush, A.; Abbaspour, M. Optimizing wave energy harvesting through oscillating water columns in semi submersible energy harvesting platforms: A comprehensive study on enhancing efficiency and competitiveness. *Ocean Eng.* **2024**, *308*, 118301. [CrossRef]
27. Kooverji, B. Pneumatic Power Measurement of an Oscillating Water Column Converter. Master's Thesis, Stellenbosch University, Stellenbosch, South Africa, 2014.
28. Falcão, A.F.O.; Henriques, J.C.C. Oscillating water column wave energy converters and air turbines: A review. *Renew. Energy* **2016**, *85*, 1391–1424. [CrossRef]
29. Falcão, A.F.O.; Henriques, J.C.C.; Gato, L.M.C.; Gomes, R.P.F. Air turbine choice and optimization for floating oscillating water column wave energy converter. *Ocean Eng.* **2014**, *75*, 148–156. [CrossRef]
30. Liu, Z.; Xu, C.; Kim, K.; Choi, J.; Hyun, B.S. An integrated numerical model for the chamber turbine system of an oscillating water column wave energy converter. *Renew. Sustain. Energy Rev.* **2021**, *149*, 111350. [CrossRef]
31. Abbasnia, A.; Rezanejad, K.; Soares, C.G. Adaptive fully nonlinear potential model for the free surface under compressible air pressure of oscillating water column devices. *Eng. Anal. Bound. Elem.* **2021**, *133*, 153–164. [CrossRef]

32. Chen, T.; Wu, B. A new frequency domain method to solve the potential flow problem. *Ocean Eng.* **2024**, *312*, 119077. [CrossRef]
33. Chen, T.; Wu, B.; You, Y.; Zhang, F. Numerical and parameterized investigation on a novel backward bent duct buoy. *Renew. Energy* **2025**, *254*, 123709. [CrossRef]
34. Taflove, A. Review of the formulation and applications of the finite difference time domain method for numerical modeling of electromagnetic wave interactions with arbitrary structures. *Wave Motion* **1988**, *10*, 547–582. [CrossRef]
35. Taghipour, R.; Perez, T.; Moan, T. Hybrid frequency time domain models for dynamic response analysis of marine structures. In Proceedings of the International Conference on Offshore Mechanics and Arctic Engineering, Estoril, Portugal, 15–20 June 2008.
36. Kim, S.J.; Koo, W.; Kim, M.H. Nonlinear time domain NWT simulations for two types of a backward bent duct buoy compared with 2D wave tank experiments. *Ocean Eng.* **2015**, *108*, 584–593. [CrossRef]
37. Penalba, M.; Giorgi, G.; Ringwood, J.V. Mathematical modelling of wave energy converters: A review of nonlinear approaches. *Renew. Sustain. Energy Rev.* **2017**, *78*, 410–423. [CrossRef]
38. Ricci, P.; Saulnier, J.B.; Falcão, A.F.O.; Pontes, M.T. Time domain models and wave energy converters performance assessment. In Proceedings of the International Conference on Offshore Mechanics and Arctic Engineering, Estoril, Portugal, 15–20 June 2008.
39. Wu, B.J.; Li, M.; Wu, R.K.; Zhang, Y.Q.; Peng, W. Experimental study on primary efficiency of a new pentagonal backward bent duct buoy and assessment of prototypes. *Renew. Energy* **2017**, *113*, 774–783. [CrossRef]